

J. Moore

T. J. Forlini

Department of Mechanical Engineering,
Virginia Polytechnic Institute and
State University,
Blacksburg, Va. 24061

A Horseshoe Vortex in a Duct

A Rankine half-body is used to model the three-dimensional flow caused by a blunt obstruction in a flow passage. The body is located in a duct bounded by two plane endwalls and two side walls shaped like potential-flow streamlines. A thick turbulent boundary layer on the endwall forms a horseshoe vortex flow as it encounters the leading edge of the body. Flow measurements are presented showing the inlet flow and the three-dimensional flow downstream of the leading edge. Sufficient data are presented for this to be a test case for the development of three-dimensional viscous flow codes.

Introduction

Computational methods for three-dimensional viscous flow are being developed [1–3] to aid turbomachinery designers in their efforts to obtain better performance and durability, and an important part of this development process involves comparison with well-documented test cases. It is the object of this paper to provide a test case for leading-edge horseshoe vortex flow. This is a feature of turbomachinery flows, especially those in turbine blade rows which must be well modeled in order to accurately model the flow in the passage downstream. Indeed the calculations of Hah [3] for a linear turbine cascade suggest that quite small discrepancies in the calculated flow near the leading edge can lead to significant differences in the location and size of the passage vortex at the exit of the cascade.

Horseshoe vortices are formed in turbomachines when annulus wall boundary layers encounter the blunt leading edges of blades and support struts. Vortex lines from the boundary layer upstream are convected and stretched around the leading edge, forming a vortex that has a characteristic horseshoe shape with streamwise vorticity downstream. The boundary layer separates from the endwall in a complex three-dimensional flow, and there is reverse flow upstream of the leading edge.

This flow is known from engine experience [4, 5] to influence the endwall thermal field and to impact on durability problems in low aspect ratio vane rows in gas turbines. So it has been the subject of many visualization studies [6–9]. But, as has been noted recently by Briley and McDonald [10], for horseshoe vortex flow “little is available in the way of detailed flow measurements . . . particularly downstream of separation.” There has not been a test case emphasizing leading-edge horseshoe vortex flow and suitable for testing turbomachinery flow codes.

The well-defined geometry of inviscid flow around a Rankine half-body provides the basis for the present study. The Rankine half-body is a thick obstruction with a rounded

nose which can interact with an endwall boundary layer to produce large flow disturbances [11]. The well-known potential flow solution provides a primary velocity distribution upon which the secondary horseshoe vortex flow is imposed.

The body is placed between the parallel endwalls of a duct to model the situation in a turbomachine where struts and blades extend over the total passage height. The Rankine half-body duct then simulates the situation found in turbomachinery passages without the complication of cascade geometry, which introduces other flow phenomena due to curvature, acceleration of the flow, and trailing edges; it exhibits three-dimensional flow due solely to the horseshoe vortex.

In this paper, quantitative flow measurements are presented to define

- (a) The inlet flow field upstream of the leading edge
- (b) The static pressure distribution on the endwall and on the surface of the body
- (c) The three-dimensional flow on two planes just downstream of the leading edge
- (d) The exit flow field far downstream

These measurements are intended to provide experimental data in a well-defined flow field for testing calculation methods for three-dimensional turbulent flows in turbomachinery blade rows.

Duct Design

Figure 1 shows a schematic view of the Rankine half-body duct with overall dimensions. The duct is 1.19 m long with endwalls spaced 0.254 m apart. The duct side walls conform to potential-flow streamlines with no allowance for displacement due to boundary layers; at the inlet, the duct width is 0.356 m. The source location, 0.508 m downstream of the duct inlet, is at the origin of the cartesian coordinate system.

Rankine Half-Body—Potential Flow

The potential flow field is defined by the superposition of a line source of strength m in a uniform flow with velocity U_∞ .

Contributed by the Gas Turbine Division of THE AMERICAN SOCIETY OF MECHANICAL ENGINEERS and presented at the 29th International Gas Turbine Conference and Exhibit, Amsterdam, The Netherlands, June 4–7, 1984. Manuscript received at ASME Headquarters January 18, 1984. Paper No. 84-GT-202.

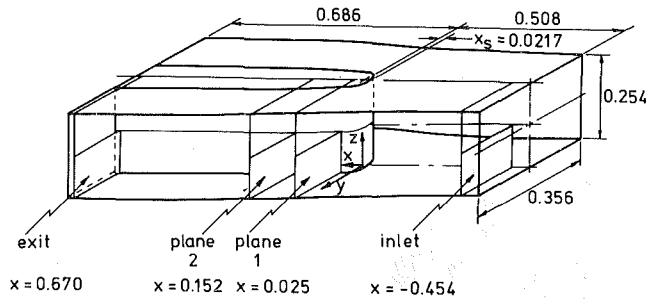


Fig. 1 Schematic of Rankine half-body duct showing measurement planes and overall dimensions in meters. Coordinate system origin located at source position.

In polar coordinates, the stream function ψ , as given by Vennard and Street [12] is

$$\psi = U_{\infty} r \sin \theta + m\theta/2\pi \quad (1)$$

Following the development in Vennard and Street, the length from the source to the stagnation point on the leading edge of the body is determined by

$$x_s = m/(2\pi U_{\infty}) \quad (2)$$

Substituting this into equation (1) gives

$$\psi/U_{\infty} = r \sin \theta + x_s \theta \quad (3)$$

which defines the potential-flow streamlines.

In the Rankine half-body duct, $x_s = 21.7$ mm. Figure 2 shows streamlines defined by equation (3) above, as well as positive values for the cartesian and polar coordinate systems located at the source position. The side walls are defined by $\psi/U_{\infty} = 7/2 \pi x_s = 0.239$ m and $\psi/U_{\infty} = -3/2 \pi x_s = -0.102$ m. The body is defined by $\psi/U_{\infty} = \pi x_s = 0.086$ m. Four intermediate streamlines defined by $\psi/U_{\infty} = 5/2 \pi x_s$, $\psi/U_{\infty} = 3/2 \pi x_s$, $\psi/U_{\infty} = 1/2 \pi x_s$, and $\psi/U_{\infty} = -1/2 \pi x_s$ are also shown in Fig. 2.

The velocity components in the axial, x , and transverse, y , directions are given by

$$u = \frac{\partial \psi}{\partial y} = U_{\infty} \left(1 + x_s \left[\frac{x}{x^2 + y^2} \right] \right) \quad (4)$$

and

$$v = -\frac{\partial \psi}{\partial x} = U_{\infty} x_s \left[\frac{y}{x^2 + y^2} \right] \quad (5)$$

and the velocity magnitude is given by

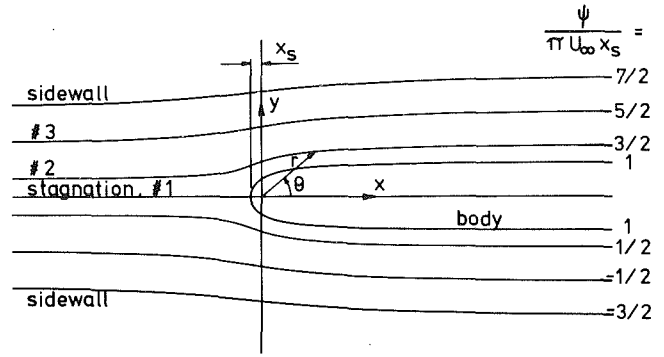


Fig. 2 Potential flow streamlines and geometry of Rankine half-body duct

$$U = \sqrt{u^2 + v^2} \quad (6)$$

Substituting the relations for u and v into equation (9) gives the velocity ratio

$$\frac{U}{U_{\infty}} = \sqrt{1 + 2x_s \left[\frac{x}{x^2 + y^2} \right] + \left[\frac{x_s^2}{x^2 + y^2} \right]} \quad (7)$$

Static Pressure Distribution—Potential Flow. A static pressure coefficient, C_{ps} , is defined as

$$C_{ps} \equiv \frac{P - P_r}{P_0 - P_r} \quad (8)$$

where P is the static pressure at the measurement point, P_0 is the upstream total pressure, and P_r is a reference static pressure. For potential flow, $P_r \equiv P_{\infty}$, the static pressure far upstream, and

$$P_0 - P_r = \frac{1}{2} \rho U_{\infty}^2 \quad (9)$$

Thus for the potential flow, the static pressure coefficient may be written as

$$C_{ps} = 1 - (U/U_{\infty})^2 \quad (10)$$

so that C_{ps} may be determined from the velocity distribution. The static pressure distribution for potential flow is given by

$$C_{ps} = -2x_s \left[\frac{x}{x^2 + y^2} \right] - \left[\frac{x_s^2}{x^2 + y^2} \right] \quad (11)$$

Figure 3 shows this theoretical static pressure distribution along the duct streamlines.

Nomenclature

C_{ps} = static pressure coefficient, $(P - P_r) / (P_0 - P_r)$
 h = duct height, 0.254 m
 H = boundary layer shape factor, δ_1 / δ_2
 m = source strength, $3.29 \text{ m}^2/\text{s}$
 P = static pressure
 P_{atm} = atmospheric pressure
 P_0 = reference total pressure measured at midheight on leading edge of body
 P_r = reference static pressure measured at midheight on sidewall where $x = -x_s/2$
 P_t = total pressure
 r, θ = polar coordinates
 R = ideal gas constant for air, 0.287 kJ/kgK

s = length along the body surface from leading edge
 T_{atm} = atmospheric temperature
 u, v, w = velocity components in cartesian coordinate directions
 U = free-stream velocity magnitude
 u' = fluctuating component of axial turbulent velocity
 U_{∞} = uniform velocity far upstream, 24.1 m/s
 x, y, z = Cartesian coordinates
 x_s = length from source to leading edge of body, $m/(2\pi U_{\infty}) = 21.7 \text{ mm}$
 δ = boundary-layer thickness, $u/U = 0.99$

δ_1 = boundary-layer displacement thickness, $\int_0^{\infty} \left(1 - \frac{u}{U} \right) dy$
 δ_2 = boundary-layer momentum thickness, $\int_0^{\infty} \frac{u}{U} \left(1 - \frac{u}{U} \right) dy$
 μ = viscosity
 ν = kinematic viscosity, μ/ρ
 ρ = density, $P_{\text{atm}}/RT_{\text{atm}}$
 ψ = stream function

Subscripts

e = exit plane
 i = inlet plane
 m = midheight in the duct

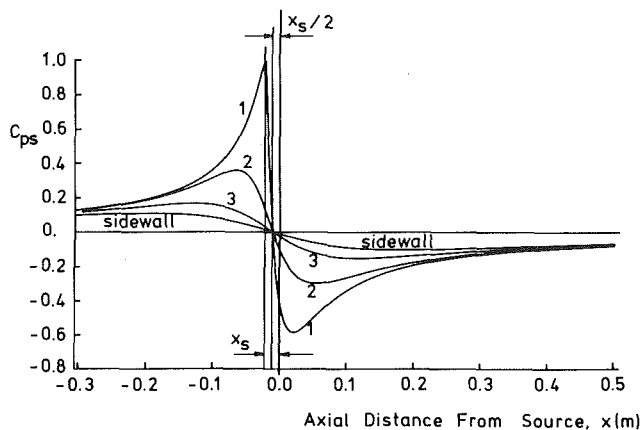


Fig. 3 Static pressure distribution for potential flow (equation (14)) along streamlines shown in Fig. 1

Figure 3 shows that far upstream and far downstream of the source at $x=0$, the static pressure in the duct approaches P_∞ . The static pressure coefficient on the stagnation and body streamline, #1, rises to unity at the leading edge of the body (stagnation point), where $x = -x_s$, and then falls around the nose of the body. The pressure coefficient reaches a minimum value of -0.59 (a maximum velocity $U/U_\infty = 1.26$) at $x = 22.9$ mm before rising to zero far downstream ($U/U_\infty = 1$). The static pressures on the other streamlines, #2, #3, and the sidewall, also fall near the leading edge and rise past the nose of the body.

One interesting feature of the static pressure distribution for the potential flow is that at $x = -x_s/2$, $P = P_\infty$ for all values of y , i.e., on all streamlines [13]. The existence of this plane of uniform static pressure allows the upstream value of static pressure, P_∞ , and velocity, U_∞ , to be measured in the duct.

Body Construction. The body is made of three 3-mm-thick plexiglass sheets formed to the Rankine half-body shape. The plexiglass walls are fastened at the top and bottom to a supporting wood frame. The frame consists of two plywood forms separated by wood supports near the body midsection, 0.254 m downstream of the leading edge of the body, and near the end of the body, 0.686 m downstream of the leading edge. The vertical seams between the plexiglass sheets are located at the forward supports, 0.254 m downstream of the leading edge, so that the nose of the body is a continuous surface. Further details of the duct and body construction are given in [13] and [14].

Wind Tunnel and Inlet Duct. The wind tunnel used as the air supply for the present tests is described by Tavakoli [15]. It ends with a straight test section 0.356 m wide, 0.254 m high and 1.24 m long. This test section was used as the inlet duct for the Rankine half-body duct. Wire screens were placed at the inlet to this section to thicken the boundary layers on the top and bottom endwalls in order to produce large horseshoe vortices at the leading edge of the Rankine half-body.

Flow Symmetry. The boundary layer screens were positioned in the tunnel to obtain a symmetrical flow at the inlet to the Rankine half-body duct. With a symmetrical flow, the amount of data necessary to define the flow are reduced, since planes of symmetry may be used as boundaries. The vertical plane along the duct centerline and the horizontal plane at the duct midheight are planes of symmetry that divide the duct into four quadrants. Care was taken to establish a symmetrical inlet flow so that data could be taken in any quadrant.

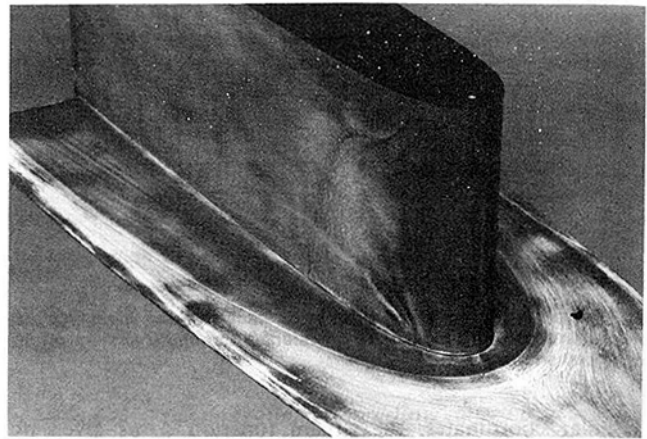


Fig. 4 Flow visualization of the limiting streamlines on the Rankine half-body and on the bottom endwall. The white dot on the top of the body, near the leading edge, is the location of the line source.

Flow Visualization

Before presenting the results of the detailed flow measurements, it is helpful to consider the overall flow development as revealed by surface flow visualization. Figure 4 shows oil-flow traces of the limiting streamlines on the horizontal (bottom) endwall of the duct and on the vertical surface of the Rankine half-body. The visualization was achieved by spraying a mixture of diesel oil and titanium dioxide onto an aluminum sheet on the endwall and onto a mylar sheet wrapped around the body; these sheets had previously been sprayed with mat black paint. The flow was then turned on for about 5 min, giving the picture shown.

The resulting flow patterns on the endwall show a classical horseshoe vortex flow that sweeps titanium dioxide away from the body revealing the dark surface beneath. The clearly defined boundary between the dark and light areas represents a line of three-dimensional flow separation which follows the vortex core.

A thin white line marks the stagnation line along the leading edge of the body. This is clearly seen at midheight, where the stagnation flow is nearly two-dimensional, but near the endwalls the horseshoe vortices induce flows which sweep the titanium dioxide towards the endwalls.

At midheight on the body, the titanium dioxide is swept around the leading edge by an apparently two-dimensional laminar boundary layer before it accumulates in a wide area which exhibits streaks vertically downwards. This is probably a region of laminar flow separation with correspondingly small shear stresses, where the oil flow is influenced by gravity. Downstream of this separation region, the oil streaks are essentially horizontal once more as the flow reattaches with a nearly two-dimensional turbulent boundary layer.

In the vicinity of the leading edge, the details of the traces on the endwall can be considered to correspond with the physical explanation of horseshoe-vortex flow given by Belik [7] and Baker [9]. In the discussion below, we have followed their procedure in marking "primary and secondary separation lines" at locations of accumulation of titanium dioxide. A close-up picture of the flow visualization in this region that shows these accumulations is given in [14] and [16]. In [16], which may be considered a companion paper to the present one, we present the results of inviscid rotational flow calculations that show reverse flow due to the horseshoe vortex upstream of the leading edge.

Flow Measurements

Measurements of the flow in the Rankine half-body duct are presented on four measurement planes normal to the duct

Table 1 Standard test conditions

P_{atm}	93.7 kPa
T_{atm}	295 K
U_{∞}	24.1 m/s
ρ_{air}	1.11 kg/m ³
μ_{air}	1.9×10^{-5} Ns/m ²
Source strength, m	3.29 m ² /s

axis (see Fig. 1) and three potential-flow streamlines defined below (see Fig. 2). Measurement of the axial flow on the inlet plane defines the inlet boundary layers on the duct endwall and side wall. Static pressure measurements on the potential-flow streamlines define the overall duct flow. Three-dimensional flow measurements on two intermediate planes downstream of the leading edge of the body define the secondary flow due to the horseshoe vortex. Measurement of the axial flow on the exit plane defines the downstream flow far from the leading edge.

Standard Test Conditions. The standard test conditions for this steady incompressible air flow and values of the fluid properties at the standard conditions are presented in Table 1. The reference static pressure, P_r , is defined as the static pressure measured on the side wall at the duct midheight where $x = -x_s/2$. This location was chosen from the potential-flow solution, presented earlier. The reference total pressure, P_0 , is defined as the stagnation pressure measured at midheight on the leading edge of the body.

Measurement Locations. Flow measurements are presented on four planes; an inlet plane at $x = -0.454$ m, two intermediate planes at $x = 0.025$ m and $x = 0.152$ m, and an exit plane at $x = 0.670$ m. Figure 1 shows the locations of the measurement planes.

The figures with the results of the measurements on the four planes show a view, looking upstream, of the measurement plane bounded by the duct walls and planes of symmetry. The location of the measurement traverses are shown as well as the origin of the duct coordinate system. Dimensions in the y -direction are given in meters, while dimensions in the z -direction are fractions of the duct height, $h = 0.254$ m. The flow measurements are presented in the quadrant of the duct defined by $z/h \leq 0.5$ and $y \geq 0$, as shown in Fig. 1.

Inlet Plane Measurements

The inlet flow distribution was measured by traversing a total pressure probe with a flattened tip on the inlet plane. Total pressure, P_t , was measured at the probe tip and static pressure, P , was measured with a static pressure tap on the endwall at the inlet plane.

Velocity Distribution. Figure 5 shows contours of axial velocity ratio, u/U_i , on the inlet plane where $U_i = 23.3$ m/s is the measured free-stream velocity. The natural boundary layer on the side wall is shown as well as the thickened boundary layer on the endwall. The endwall boundary layer is uniform over the center half of the duct width where the flow interacts with the body. The boundary layer parameters for this region are presented in Table 2, together with the parameters for the side wall at midheight. Further details are given in [14].

Turbulence Intensity. The turbulence intensity was approximated by measuring the mean and RMS signals from a

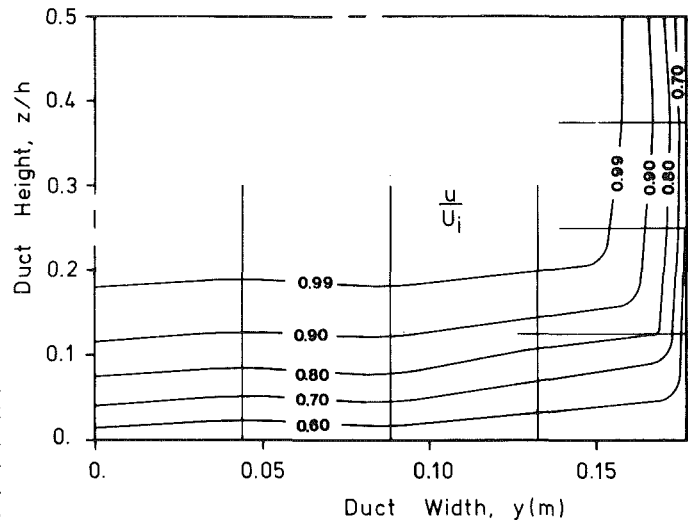


Fig. 5 Contours of axial velocity ratio (u/U_i) on the inlet plane. Free-stream velocity, $U_i = 23.3$ m/s.

Table 2 Inlet boundary layer parameters (endwall over center half of the duct width and side wall at duct midheight)

		Endwall	Sidewall
Thickness	δ	46.4 mm	19.1 mm
Displacement thickness	δ_1	9.0 mm	2.8 mm
Momentum thickness	δ_2	6.4 mm	2.1 mm
Shape Factor	H	1.42	1.30

single-wire, hot-wire anemometer that was traversed across the inlet plane. The distributions of turbulence intensity ($\sqrt{u'^2}/U_i$) in the endwall boundary layer showed little variation over the center half of the duct; the shape of the distribution in this region was quite similar to that reported by Klebanoff [17] for a turbulent boundary layer on a flat plate but the values were approximately 15 percent lower. The inlet free stream turbulence intensity was 0.5 percent of U_i .

Static Pressure Measurements

The static pressure distribution was measured with an inclined, multiple-tube manometer and also with a Statham pressure transducer. Multiple data points are shown where repeated pressure measurements gave slightly differing results.

Wall static pressure tapings are located along three of the potential-flow streamlines shown in Fig. 2. Streamline #1 is the stagnation streamline upstream of the body and the body streamline. Streamline #2 and streamline #3 are the two intermediate streamlines defined by $\psi/U_{\infty} = 3/2 \pi x_s$ and $\psi/U_{\infty} = 5/2 \pi x_s$. The static pressure taps on the stagnation streamline and on streamlines #2 and #3 are located on the duct endwall while the pressure taps on the body are located at the duct midheight. Pressure tapings are also located around the perimeter of the uniform pressure plane at $x = -x_s/2$. All of the static pressure tapings are nominally 0.5 mm dia.

Figure 6 shows the static pressure distribution measured in the duct compared with the calculated potential-flow distribution.

Stagnation Streamline. The static pressure on the stagnation streamline, measured on the endwall upstream of the body, is shown in greater detail in Fig. 7. Far from the leading edge, between 0.10 and 0.25 m upstream, the measured data deviates little from the potential flow solution. Less than 0.10 m upstream, the deviation of the measured data becomes larger with decreasing distance from the leading edge, ending at a stagnation value of $C_{ps} = 0.85$. This

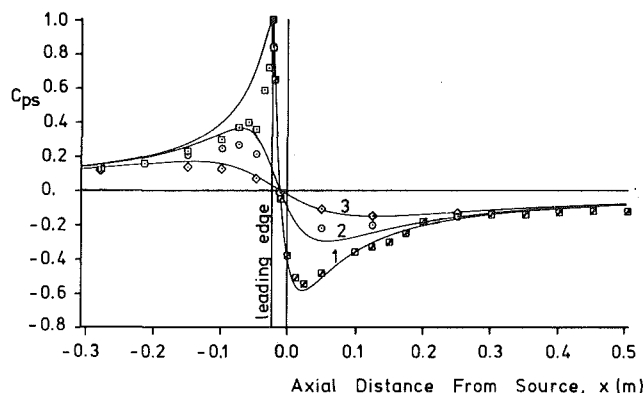


Fig. 6 Wall static pressure distributions along streamlines shown in Fig. 1: — potential flow, equation (14); □, measurements on endwall for streamline 1; ○, measurements at midheight on body for streamline 1; ◇, measurements on endwall for streamline 2; ◇, measurements on endwall for streamline 3

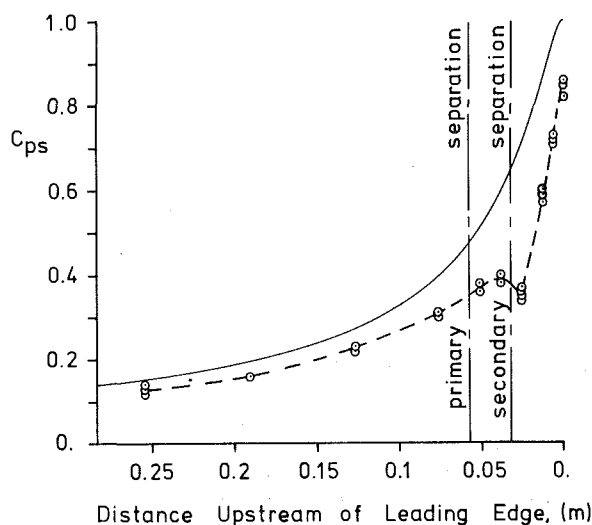


Fig. 7 Wall static pressure distribution along stagnation streamline (1) on duct endwall: — potential flow, equation (14); - - - mean line through data, 0; - · - saddle points of separation

low stagnation value may be due to low-velocity, boundary-layer fluid stagnating at the junction of the leading edge and the endwall.

A local minimum in the measured static pressure occurs 0.025 m upstream of the leading edge. This minimum has been assumed by Belik [7] to be adjacent to the core of the horseshoe vortex. From endwall flow visualization, the location of the secondary separation line, which according to Belik follows the course of the vortex core, was found to be 0.032 m upstream of the leading edge of the body; primary separation occurred 0.057 m upstream of the leading edge; the locations of the two separation saddle points are marked on Fig. 7. It is interesting to note the local peak in static pressure between the two saddle points; this is probably associated with a nodal point of reattachment [9].

Body Streamline. Figure 8 shows the static pressure distribution measured at midheight along the body. The measurements show the flow accelerating around the nose to a minimum of $C_{ps} = -0.54$ at $x = 0.025$ m, which corresponds to $U/U_\infty = 1.24$. This is compared to the potential flow maximum $U/U_\infty = 1.26$ at $x = 0.023$ m. The measured flow then decelerates to a relatively constant value of $C_{ps} = -0.12$ for $x > 0.3$ m; this small variation of static pressure may be due to the increasing displacement thickness of the wall boundary layers.

The region between $x = 0.10$ m and $x = 0.30$ m is in-

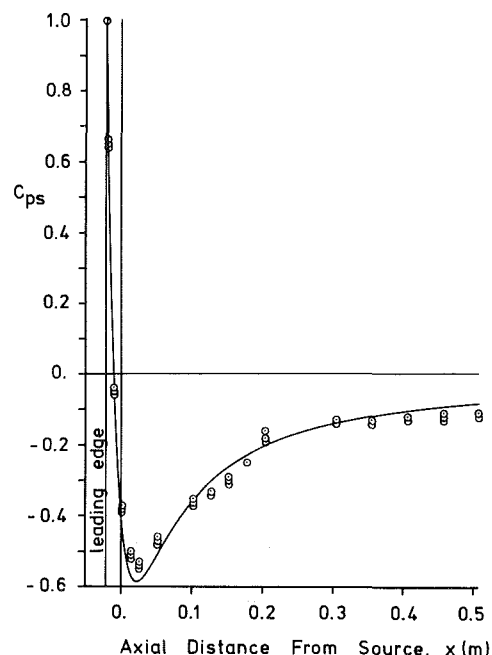


Fig. 8 Wall static pressure distribution at midheight on body: — potential flow, equation (14); ○, measurements

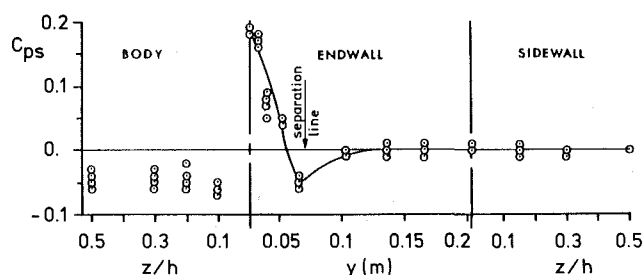


Fig. 9 Wall static pressure distribution on theoretical uniform-pressure plane at $x = -x_s/2$

teresting. The data points measured in this region suggest boundary-layer separation and reattachment, as discussed by Schlichting [18]. There is a section of slight pressure rise, which is less than for the potential flow solution, instead of the constant pressure described by Schlichting. Then there is a larger pressure rise that overshoots the potential flow solution before returning to the nearly constant downstream static pressure.

The construction of the body prevented measurements between $x = 0.20$ m and $x = 0.30$ m. The wood supports did not allow access to the body surface for a pressure tap, and the vertical seam between the plexiglass sheets was located here. The static pressure measurements on the body were unchanged when the vertical seam was covered with cellophane tape, so that the presence of the seam was not a probable cause for the flow disturbance. This region of the flow will be discussed further in the section that describes the calculation of the boundary layer on the body.

Uniform-Pressure Plane. Figure 9 shows the static pressure distribution measured around the perimeter of the theoretical uniform-pressure plane at $x = -x_s/2$. The value of C_{ps} at midheight on the sidewall is by definition equal to zero. The measured C_{ps} is uniform and equal to zero on the side wall and on the outer 60 percent of the endwall away from the body. C_{ps} decreases to a minimum of approximately

-0.05 at $y = 0.064$ m just inside the separation line at $y = 0.072$ m; it then increases to 0.18 at the junction of the body and endwall. The measured value of C_{ps} on the body is relatively uniform at about -0.05; this does not seem to be related to the endwall minimum, since the velocity gradient is large here and an error in C_{ps} of ± 0.05 corresponds to an error in the placement of the static pressure tap on the body of only ± 0.8 mm measured in the axial direction.

Secondary Flow Measurements

The flow distribution just downstream of the leading edge was determined by traversing a five-hole pressure probe on plane 1, at $x = 0.025$ m, and on plane 2, at $x = 0.152$ m.

Pressures were measured relative to the reference static pressure, P_r , at midheight on the side wall where $x = -x_s/2$. The static pressure, $P - P_r$, total pressure, $P_t - P_r$, pitch angle, measured in the vertical plane, and yaw angle, measured in the horizontal plane, were obtained from the five-hole probe measurements; and from these results, the three velocity components u , v , and w in the x -, y -, and z -directions, respectively, were calculated.

Method of Presenting Secondary Velocities. The secondary velocities and the corresponding velocity vectors for planes 1 and 2 are shown in Figs. 10-13. In order to present the data alone, the v components of velocity from the potential flow are not subtracted from the measured v values. This would involve the reader in calculating the local value of v for the potential flow and then correcting each point on the figures in order to obtain the actual measured values for v . Instead, the data are presented as $v - v_m$, where v_m is the measured v velocity at midheight ($z/h = 0.5$) for the particular vertical traverse considered. At each plane there are seven vertical traverses, and with this method of plotting the data, all the values, $v - v_m$, go to zero at midheight; the plots then show variations in secondary velocity relative to the value at midheight. At the endwall, all the velocity components are zero, and the value of $v - v_m$ plotted is simply $-v_m$, the negative of the velocity component v_m for that traverse at midheight.

Velocities at Midheight. The measured velocities at midheight were compared with the corresponding values from potential flow theory, found using equations (2), (4), and (5), with the source strength m and the free stream velocity U_∞ from Table 1.

At plane 1, the measured axial velocity component u/U_∞ was slightly higher by 1.1 percent ± 0.5 percent; at plane 2, the inner six points were consistently higher in u/U_∞ , 2.3 percent ± 0.4 percent, while the outer point agreed with the potential flow value.

Apart from one point, the measured values of velocity component v at midheight were consistently less than those calculated from potential flow theory. At plane 1, all the values were smaller by -0.3 m/s ± 0.2 m/s and at plane 2 the outer six values were smaller by -0.4 m/s ± 0.1 m/s. This suggests a small secondary flow towards the body at midheight. The only point which showed a secondary flow away from the body at midheight was the point next to the body at plane 2. As discussed in the boundary layer section, below, this point was adjacent to a region of laminar flow separation on the body which may explain the small positive secondary velocity of 0.1 m/s (relative to the potential flow) and the significant difference of this point from the others at plane 2.

Secondary Velocities. The y and z components of secondary velocity, $v - v_m$ and w , on plane 1, at $x = 0.025$ m, are shown in Fig. 10. The velocity in the y -direction shows a

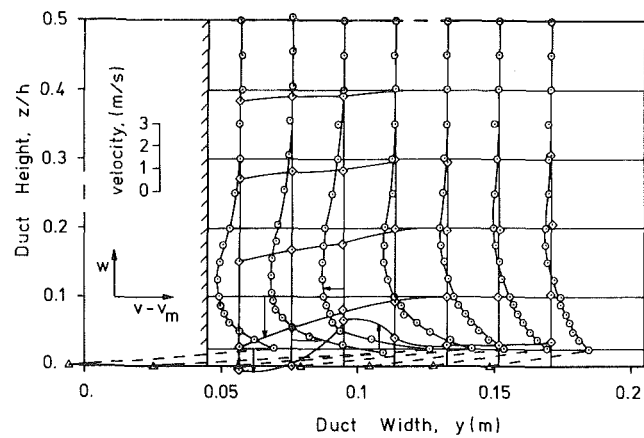


Fig. 10 Secondary velocities measured on plane 1: v_m = component of velocity in y -direction measured at midheight. Velocity components: \circ , $v - v_m$; \diamond , w ; Δ , $v - v_m = -v_m$ at wall.

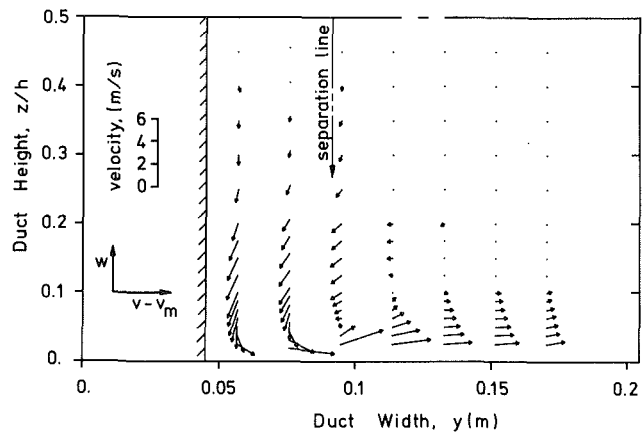


Fig. 11 Secondary velocity vectors measured on plane 1. v_m = component of velocity in y -direction measured at midheight.

region near the endwall where v is greater than v_m then a region where v is less than v_m before reaching the midheight value, v_m . The secondary flow in the y -direction extends approximately 30 percent of the duct height from the endwall. The maximum measured value of $v - v_m$ is 4.0 m/s at $y = 0.076$ m, $z/h = 0.019$. At this y -station v_m is 6.1 m/s and u_m is 26.4 m/s.

The velocity in the z -direction shows flow towards the endwall near the body. At $z/h = 0.025$, there is a flow reversal between $y = 0.076$ m, where $w = -0.8$ m/s, and $y = 0.095$ m, where $w = 1.3$ m/s, which indicates the presence of the vortex with counterclockwise rotation. This is the direction of rotation associated with the boundary-layer vortex line stretched around the body.

Figure 11 shows the corresponding vector plot illustration of the secondary velocities on plane 1. Vectors with magnitudes less than 0.30 m/s are considered insignificant and are not shown. The location of the separation line on the endwall, at $y = 0.092$ m, is indicated on Fig. 11.

The secondary velocities, $v - v_m$ and w , on plane 2, at $x = 0.152$ m, are shown in Fig. 12. The region of secondary flow in the y -direction is limited to the 10 percent of the duct height near the endwall. Secondary flow away from the body is seen in this region. The secondary flow towards the body, seen on plane 1, is less significant on this plane. The maximum measured value of $v - v_m$ is 4.3 m/s, which occurs at $y = 0.133$ m and $z/h = 0.025$. At this y -station, v_m is 1.3 m/s and u_m is 26.6 m/s.

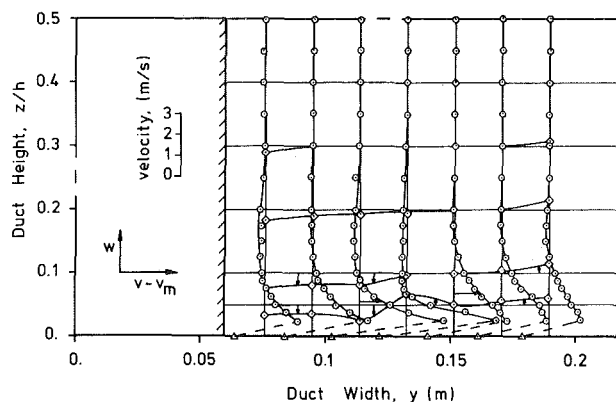


Fig. 12 Secondary velocities measured on plane 2. v_m = component of velocity in y -direction measured at midheight. Velocity components: $0, v-v_m$; \diamond, w ; $\Delta, v-v_m = -v_m$ at wall.

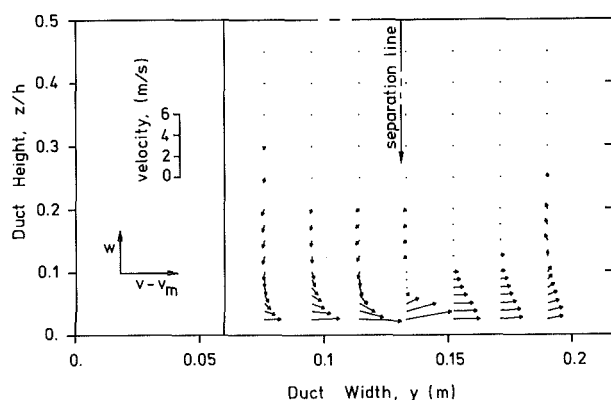


Fig. 13 Secondary velocity vectors measured on plane 2

The secondary flow in the z -direction is towards the end-wall near the body, as seen before. The flow reversal, which indicates the presence of the vortex, can be seen at $z/h = 0.05$, between $y = 0.114$ m, where $w = -0.8$ m/s, and $y = 0.133$ m, where $w = 0.5$ m/s. The vector plot in Fig. 13 illustrates these secondary velocities on plane 2.

Exit Plane Measurements

The exit flow distribution was measured as at the inlet by traversing the total pressure probe with a flattened tip on the exit plane. Total pressure, P_t , was measured at the probe tip. Static pressure, P , was measured with the static pressure portion of a pitot-static tube. The static pressure was measured at a single point in the free stream, since the exit static pressure was found to be uniform.

Velocity Distribution. Figure 14 shows the distribution of the exit velocity as a fraction of the exit free-stream velocity, u/U_e , where $U_e = 25.7$ m/s. The boundary layer on the body is approximately 11 mm thick and is uniform over the center 60 percent of the duct height. The boundary layer on the endwall is thinnest in the region near the junction of the body and the endwall. The endwall boundary layer profiles show a thin inner layer that reaches a constant velocity less than U_e , then an outer layer, that increases in velocity to U_e . Exit endwall boundary layer profiles are shown in Fig. 15. The dashed line on Fig. 14 shows the location of the edge of the inner endwall boundary layer.

The fluid near the edge of the outer endwall boundary layer at the exit plane is most likely from the thickened endwall boundary layer at the inlet, while the inner boundary layer

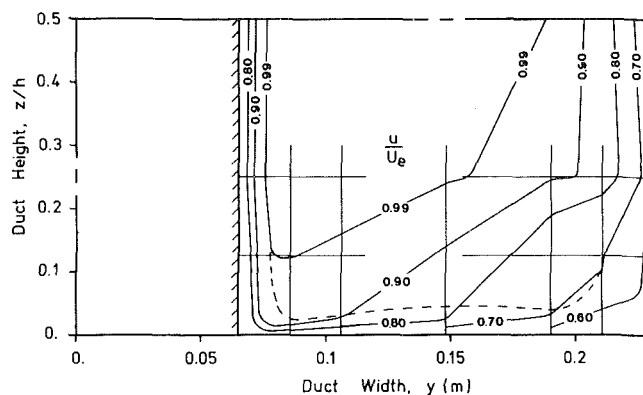


Fig. 14 Contours of axial velocity ratio (u/U_e) on the exit plane. Free-stream velocity, $U_e = 25.7$ m/s.

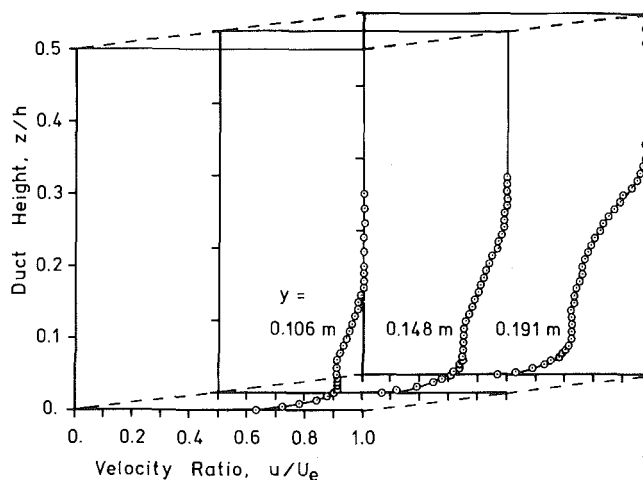


Fig. 15 Axial velocity profiles on the endwall at the exit plane

originates midway along the duct, possibly downstream of the horseshoe vortex, behind the secondary separation line (the dark area on the endwall in Fig. 4). This situation is analogous to that reported by Langston, Nice, and Hooper [19], where the endwall boundary layer in the turbine cascade grows downstream of the separation line.

Boundary-Layer Analysis

A two-dimensional analysis was performed for the boundary layer on the body at duct midheight. The boundary layer analysis consists of a numerical laminar calculation around the nose of the body, and a flat-plate turbulent approximation after transition. The velocity distribution from the static pressure measurements on the body was used as the free stream, which must be known for the laminar calculation. The assumption of steady, incompressible flow is made in this analysis.

Laminar Integral Calculation

The laminar boundary layer was calculated using an integral technique [20] similar to that given by Tani [21]. It uses the momentum and mechanical-energy integral equations to solve for the shape factor, H , and the momentum thickness, δ_2 , as a function of the distance, s , measured along the body surface from the leading edge.

Turbulent Flat-Plate Calculation

The well-known relation for the momentum thickness of a flat-plate turbulent boundary layer was used for the turbulent

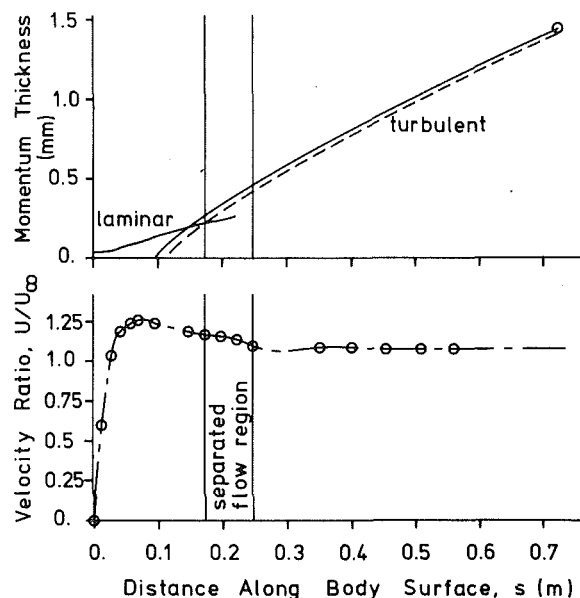


Fig. 16 Results of two-dimensional boundary layer calculation at midheight on body: — laminar and flat-plate turbulent boundary layer calculations to match measured momentum thickness (δ) at exit; - - - flat-plate calculation from separation line found by flow visualization; - · - curve fit of free-stream velocity ratio (from measured wall static pressures) used in laminar boundary layer calculation; $U_\infty = 24.1$ m/s

calculation [22]. The exit velocity, $U_e = 25.7$ m/s, was the constant free-stream velocity imposed on the boundary layer.

The turbulent layer momentum thickness was calculated using the measured δ_{2e} as a known endpoint. This produced a flat-plate distribution which resulted in the measured δ_{2e} at the exit plane. Another calculation was performed using the value of δ_2 from the laminar calculation as a known initial condition at a chosen transition point.

Calculation Results

Figure 16 shows the momentum thickness calculated at midheight on the body. The measured velocity distribution is shown to the same scale for reference. The separated flow region, inferred from the measured static pressure distribution and flow visualization, is shown between $s = 0.17$ m and $s = 0.25$ m.

The two-dimensional laminar boundary layer calculation shows separation at $s = 0.22$ m, using $H = 4.029$ as the laminar separation criterion. The calculated laminar separation point is downstream of the inferred separation point, but upstream of the inferred reattachment point.

The turbulent flat-plate boundary layer calculation from the measured exit value of $\delta_2 = 1.45$ mm is shown as the solid line in Fig. 16. This calculated curve intersects the laminar curve at $s = 0.15$ m, showing an effective transition point upstream of the inferred separation region.

An effective transition point at the inferred separation point, at $x = 0.17$ m, was obtained by matching the momentum thickness from the turbulent boundary layer calculation to the momentum thickness from the laminar boundary layer calculation. The result of this calculation is shown as the dashed line in Fig. 16 and gives an exit value of $\delta_2 = 1.40$ mm. The difference between this calculated exit momentum thickness and the exit momentum thickness from the measurements is only 3.5 percent of the measured value.

Summary

This paper has presented measurements of the three-

dimensional flow in a duct due to the horseshoe vortex at the junction of the duct endwall and a Rankine half-body obstruction. The inlet boundary layer on the duct endwall was artificially thickened to produce a relatively large horseshoe vortex. Measurements on four planes normal to the duct axis define the flow for comparison with the results of three-dimensional viscous flow calculation procedures. A symmetrical flow field was obtained to reduce the amount of measurement and subsequent calculation necessary to determine the duct flow.

A two-dimensional potential-flow analysis shows that at an axial location halfway between the source and the leading edge of the body, the velocity on all streamlines in the duct is equal to the uniform velocity upstream. The static pressure was measured on the duct walls around the perimeter of the plane at this axial location and found to be uniform except near the junction of the body and the duct endwall. In this corner region, the horseshoe vortex influenced the flow.

Variations in endwall static pressure upstream of the leading edge of the body are related to details of the horseshoe vortex flow. A local minimum in static pressure occurs near the saddle point on secondary separation, and a local maximum occurs between the saddle points of primary and secondary separation near a nodal point of reattachment.

Secondary flow velocities just downstream of the leading edge show the streamwise vorticity associated with the horseshoe vortex. The secondary velocities are largest near the endwall where the secondary flow is away from the body; at the duct midheight, a small secondary flow is observed towards the body. The core of the vortex occurs just inside the separation line on the endwall.

Velocity profiles measured on the exit plane show an inner boundary layer on the duct endwall. This result is similar to results reported in turbine cascades, where a new endwall boundary layer starts downstream of flow separation near the leading edges of the blades.

The two-dimensional laminar boundary layer calculation at midheight on the body predicts separation downstream of the location where static pressure measurements show characteristics of boundary layer separation. The boundary layer momentum thickness calculated by the laminar technique at the measured separation point was used to start a flat-plate turbulent boundary layer calculation. The exit momentum thickness calculated in this manner differed from the momentum thickness determined from the measured exit boundary layer by only 3.5 percent of the measured value.

References

- 1 Dodge, P. R., "Numerical Method for 2D and 3D Viscous Flows," AIAA Paper No. 76-425, 1976.
- 2 Moore, J. G., and Moore, J., "Lecture Notes on the Calculation of Three-Dimensional Viscous Flows Using Pressure Correction Methods," ASME Gas Turbine Division Short Course on 3-D Flows in Turbomachinery Blade Rows, Phoenix, Arizona, Mar. 1983.
- 3 Hah, C., "A Navier-Stokes Analysis of Three-Dimensional Turbulent Flow Inside Turbine Blade Rows at Design and Off-Design Conditions," ASME Paper No. 83-GT-40, 1983.
- 4 York, R. E., Hylton, L. D., and Mihelc, M. S., "An Experimental Investigation of Endwall Heat Transfer and Aerodynamics in a Linear Vane Cascade," ASME Paper No. 83-GT-52.
- 5 Gaugler, R. E., and Russell, L. M., "Comparison of Visualized Turbine Endwall Secondary Flows and Measured Heat Transfer Patterns," ASME Paper No. 83-GT-83.
- 6 Schwind, R. G., "The Three-Dimensional Boundary Layer Near a Strut," MIT Gas Turbine Laboratory Report No. 67, May 1962.
- 7 Belik, L., "The Secondary Flow About Circular Cylinders Mounted Normal to a Flat Plate," *Aeronautical Quarterly*, Vol. 24, No. 1, Feb. 1973, pp. 47-54.
- 8 Barber, T. J., "An Investigation of Strut-Wall Intersection Losses," *Journal of Aircraft*, Vol. 15, No. 10, Oct. 1978, pp. 676-681.
- 9 Baker, C. J., "The Turbulent Horseshoe Vortex," *Journal of Wind*

Engineering and Industrial Aerodynamics, Vol. 16, Nos. 1 and 2, July 1980, pp. 9-23.

10 Briley, W. R., and McDonald, H., "Computation of Three-Dimensional Horseshoe Vortex Flow Using the Navier Stokes Equations," Seventh International Conference on Numerical Methods in Fluid Dynamics, Stanford University & NASA/Ames, June 23-27, 1980.

11 Hawthorne, W. R., "The Secondary Flow About Struts and Airfoils," *Journal of the Aeronautical Sciences*, Vol. 21, No. 9, Sept. 1954, pp. 588-608.

12 Vennard, J. K., and Street, R. L., *Elementary Fluid Mechanics*, 5th ed., John Wiley & Sons, 1976, pp. 608-610.

13 Boblitt, W. W., "Horseshoe Vortices in a Duct," B.S. thesis, VPI&SU, June 1982.

14 Forlini, T. J., "Measurement of Three-Dimensional Horseshoe Vortex Flow in a Duct," M.S. thesis, VPI&SU, June 1983.

15 Tavakoli, A., "Design and Evaluation of a Pulsating Flow Wind Tunnel," M.S. thesis, VPI&SU, Sept. 1982.

16 Moore, J. G., and Moore, J., "Calculation of Horseshoe Vortex Flow Without Numerical Mixing," ASME Paper No. 84-GT-241.

17 Klebanoff, P. S., "Characteristics of Turbulence in a Boundary Layer with Zero Pressure Gradient," NACA Report 1247, 1955.

18 Schlichting, H., *Boundary Layer Theory*, 7th ed., McGraw-Hill, 1979, p. 220.

19 Langston, L. S., Nice, M. L., and Hooper, R. M., "Three-Dimensional Flow Within a Turbine Cascade Passage," *JOURNAL OF ENGINEERING FOR POWER*, Vol. 99, No. 1, Jan. 1977, pp. 21-28.

20 Moses, H. L., Unpublished notes, VPI&SU, Winter 1982.

21 Tani, I., "On the Approximate Solution of the Laminar Boundary Layer Equations," *Journal of Aeronautical Sciences*, Vol. 21, No. 7, July 1954, pp. 487-495.

22 Schlichting, H., *Boundary Layer Theory*, 7th ed., McGraw-Hill, 1979, pp. 636-638.